# Supporting Information

## Single Ru atoms with precise coordination on monolayer layered double hydroxide for efficient electrooxidation catalysis

Zelin Wang,‡[a] Si-Min Xu,‡[a] Yanqi Xu,[a] Ling Tan,[a] Xian Wang,[a] Yufei Zhao,*[a] Haohong Duan,*[b] and Yu-Fei Song*[ac]

*a. State Key Laboratory of Chemical Resource Engineering, Beijing University of Chemical Technology, Beijing 100029 P. R. China.*
*b. Department of Chemistry, University of Oxford, 12 Mansfield Road, Oxford, OX1 3TA, U.K.*
*c. Beijing Advanced Innovation Center for Soft Matter Science and Engineering, Beijing University of Chemical Technology, Beijing 100029 P. R. China.*

## Contents

# Section 1. Experimental Detail

***Chemicals:*** $Ni(NO_3)_2 \cdot 6H_2O$ (99%), $Fe(NO_3)_3 \cdot 9H_2O$ (99%), $NaNO_3$ (>98%), NaOH (>98%), $RuCl_3 \cdot 3H_2O$ (99%), Formamide (99%), $NH_4F$ (>98%), urea (99%) and all used solvents (analytical grade) were obtained from Energy Chemical and were used directly without any further purification.

***Characterization:*** High resolution transmission electron microscopy (HRTEM) images were collected on a JEOL JEM-2010 electron microscope. High-angle annular dark-file scanning trans-mission electron microscopy (HAADF-STEM) images were collected on JEOL JEM-ARM200F microscope incorporated with a spherical aberration correction system for STEM. Energy-dispersive X-ray spectroscopy (EDS) mapping was performed using a 100 $mm^2$ JEOL Centurio SDD EDS detector. Atomic Force Microscope (AFM) was collected on Multimode Nanoscope IIIa, Veeco Instruments. Inductively coupled plasma atomic emission spectroscopy (ICP-AES) analysis was performed on a Shimadzu ICPS-7500 instrument. K-edge XANES measurements were performed at the 1W1B beamline of Beijing Synchrotron Radiation Facility. Fourier transform EXAFS (FT-EXAFS) shell fitting was carried out with Artemis Software.[1] wavelet transform EXAFS (WT-EXAFS) was analysis through Continuous Cauchy Wavelet Transform (CCWT).[2] X-ray photoelectron spectroscopy (XPS) measurements were explored with monochromatized Al K exciting X-radiation (PHI Quantera SXM). Powder X-ray diffraction (XRD) analysis was recorded on a Bruker D8 diffractometer with Cu-K$\alpha$ radiation. $N_2$ adsorption-desorption isotherms were measured using Quantachrome Autosorb-1 system at liquid nitrogen temperature. Faradaic efficiency was quantified by gas chromatography (Shimadzu GC 2014C, TCD detector, He as carrier gas).

***Synthesis of mono-NiFe:*** The mono-NiFe was prepared *via* one-step coprecipitation method according to the reference with slightly modification.[3] A 20.0 mL solution composed of 0.75

mmol $Ni(NO_3)_2 \cdot 6H_2O$ and 0.25 mmol $Fe(NO_3)_3 \cdot 9H_2O$ was added drop by drop to a solution of 20.0 mL $NaNO_3$ (0.010 M) containing 23 vol% formamide. Simultaneously, 0.25 M NaOH was added dropwise to maintain the system at a pH value of ca. 10 under magnetic stirring at 80 °C. The reaction was completed within 10 min. The precipitates were collected by centrifugation, washed with water and ethanol for more than 3 times.

***Synthesis of $Ru_1$/mono-NiFe-x (x = 0.3, 1.6, 3.8, 7.0):*** A 20.0 mL solution composed of 0.75 mmol $Ni(NO_3)_2 \cdot 6H_2O$, 0.25 mmol $Fe(NO_3)_3 \cdot 9H_2O$ and different amount of $RuCl_3 \cdot 3H_2O$ was added dropwise to a solution of 20.0 mL $NaNO_3$ (0.010 M) containing 23 vol% formamide. Simultaneously, under magnetic stirring a solution of 0.25 M NaOH was added dropwise to maintain the system at a pH value of ca. 10 at 80 °C. The reaction was completed within 10 min. The precipitates were collected by centrifugation, washed with water and ethanol for more than 3 times. The prepared catalysts were denoted as $Ru_1$/mono-NiFe-*x* (*x* = 0.3, 1.6, 3.8, 7.0) corresponding to the $RuCl_3 \cdot 3H_2O$ amount of 3.75 μmol, 22.5 μmol, 62.5 μmol and 125 μmol, respectively.

***Synthesis of bulk-NiFe:*** bulk-NiFe was synthesis through hydrothromal method. 6.0 mmol $Ni(NO_3)_2 \cdot 6H_2O$ (1.74 g), 2.0 mmol $Fe(NO_3)_3 \cdot 9H_2O$ (0.808 g), 40.0 mmol urea (2.40 g) and 16.2 mmol $NH_4F$ (0.60 g) were dissolved in 80 mL $H_2O$, and then transferred to a Teflon-lined autoclave at 120 $^oC$ for 25 h.

***Synthesis of $Ru_1$/mono-NiAl:*** A 20.0 mL solution composed of 0.75 mmol $Ni(NO_3)_2 \cdot 6H_2O$, 0.25 mmol $Al(NO_3)_3 \cdot 9H_2O$ and 3.75 μmol $RuCl_3 \cdot 3H_2O$ was added dropwise to a solution of 20.0 mL $NaNO_3$ (0.010 M) containing 23 vol% formamide. Simultaneously, under magnetic stirring a solution of 0.25 M NaOH was added dropwise to maintain the system at a pH value of ca. 10 at 80 °C. The reaction was completed within 10 min. The precipitates were collected by centrifugation, washed with water and ethanol for more than 3 times.

***Synthesis of $Ru_1$/mono-MgAl:*** A 20.0 mL solution composed of 0.75 mmol $Mg(NO_3)_2 \cdot 6H_2O$, 0.25 mmol $Al(NO_3)_3 \cdot 9H_2O$ and 3.75 μmol $RuCl_3 \cdot 3H_2O$ was added drop by drop to a solution

of 20.0 mL $NaNO_3$ (0.010 M) containing 23 vol% formamide. Simultaneously, under magnetic stirring a solution of 0.25 M NaOH was added dropwise to maintain the system at a pH value of ca. 10 at 80 °C. The treatment is the same as above.

***Synthesis of $Ru_1$/Urea-NiFe-0.6:*** $Ru_1$/Urea-NiFe-0.6 was synthesis through hydrothromal method. 6.0 mmol $Ni(NO_3)_2 \cdot 6H_2O$ (1.74 g), 2.0 mmol $Fe(NO_3)_3 \cdot 9H_2O$ (0.808 g), 40.0 mmol urea (2.40 g), 16.2 mmol $NH_4F$ (0.60 g) and 1.0 mmol $RuCl_3 \cdot 3H_2O$ (0.27 g) were dissolved in 80 mL $H_2O$, and then transferred to a Teflon-lined autoclave at 120 $^oC$ for 25 h.

***Electrochemical tests:*** Electrodes were tested on a CHI 760E electrochemical workstation (Shanghai Chenhua Instrument Co., China) in a three-electrode electrochemical cell using a 1 M KOH and 0.2 M $N_2H_4$ aqueous solution as electrolyte at room temperature. The working electrode was prepared by loading 1 mg sample on 1 cm × 1 cm area carbon paper. A Pt wire and a saturated calomel electrode (SCE) were used as the counter and reference electrode, respectively. The distance between the working electrode and the counter electrode was 2 cm. In the hydrazine oxidation reaction, the linear sweep voltammetry (LSV) curves were recorded at a scan rate of 5 mV $s^{-1}$. AC impedance measurements were carried out in the same configuration at 0.23 V *vs*. SCE from 0.01 Hz to 100 KHz with an AC voltage of 5 mV. Hence, a series of cyclic voltammetry (CV) measurement were performed at various scan rates (5, 10, 20, 30, 60 mV $s^{-1}$) from –0.25 to –0.20 V *vs*. SCE, and the sweep segments of the measurements were 30. The stability tests were operated through CV measurement with a scan rate of 30 mV $s^{-1}$.

***Computational details:***

The primitive model for NiFe-LDH was built with the space group of $p\bar{3}m1$, indicating that $a = \beta = 90^o$, $\gamma = 120^o$. The other three lattice parameters, *a*, *b*, and *c*, were referred to the powder X-ray diffraction pattern. The supercell of NiFe-LDH was 4 × 4 × 1 in the *a*-, *b*-, and *c*-directions. The molar ratio of $Ni^{2+}$: $Fe^{3+}$ in LDH matrix was 3. Nitrate anion was placed in the

interlayer space of NiFe-LDH to keep the model neutral. The model of bulk-NiFe was obtained by cleaving the (003) surface of NiFe-LDH. This model contained two bilayers of LDH matrix and interlayer anion. The chemical formula of bulk-NiFe was $Ni_{24}Fe_8(OH)_{64}(NO_3)_8$. The model of mono-NiFe contained one bilayer of LDH matrix and interlayer anion, together with one oxygen vacancy. The chemical formula of mono-NiFe was $Ni_{12}Fe_4(OH)_{31}(NO_3)_4$. The model of $Ru_1$/mono-NiFe was built by adding a Ru atom above the Fe atom in mono-NiFe, resulting in the chemical formula of $Ni_{12}Fe_4(RuO_4H)(OH)_{28}(NO_3)_4$.

In present work, the density functional theory (DFT) calculations were performed using a plane wave implementation[4] with the CASTEP (Accelrys Software Inc., San Diego, CA).[5] The exchange and correlation were described with the Perdew-Burke-Ernzerhof (PBE) functional in generalized gradient approximation (GGA).[6] Spin-polarized DFT + U theory was applied for the transition metals (Ni, Fe, and Ru here). The values of $U - J$ ($U_{eff}$) were 3.80 eV for $Ni^{2+}$,[7, 8] 4.30 eV for $Fe^{3+}$,[9] and 4.10 eV for $Ru^{3+}$,[10] respectively. The ionic cores were described with the ultrasoft pseudopotentials to improve transferability and reduce the number of plane waves required in the expansion of Kohn-Sham orbitals.[11, 12] The potential energy surface was searched using the Broyden-Fletcher-Goldfarb-Shanno (BFGS) algorithm.[13] The cutoff energy was set to be 380 eV.[14] The structure optimization was based on the following three points: (a) an energy tolerance of $2 \times 10^{-5}$ eV/atom, (b) a force tolerance of 0.05 eV/Å, and (c) a displacement tolerance of $2 \times 10^{-3}$ Å.

The energy of Ru atoms located upon the Ni, O and Fe (denoted as $E_{Up\text{-}Ni}$, $E_{Up\text{-}O}$ and $E_{Up\text{-}Fe}$). We select $E_{Up\text{-}Ni}$ as reference energy because of $E_{Up\text{-}Ni}>E_{Up\text{-}O}>E_{Up\text{-}Fe}$. The Relative energy of Ru atoms located upon the Ni, O and Fe (denoted as $E_{R\text{-}Up\text{-}Ni}$, $E_{R\text{-}Up\text{-}O}$ and $E_{R\text{-}Up\text{-}Fe}$) was calculated with eqs 1-3:

$$E_{R\text{-}Up\text{-}Ni} = E_{Up\text{-}Ni} - E_{Up\text{-}Ni} \quad (1)$$

$$E_{R\text{-}Up\text{-}O} = E_{Up\text{-}O} - E_{Up\text{-}Ni} \quad (2)$$

$$E_{\text{R-Up-Fe}} = E_{\text{Up-Fe}} - E_{\text{Up-Ni}} \quad (3)$$

The isosurfaces of mono-NiFe and $Ru_1$/mono-NiFe are analyzed with the value of 0.004 $e$Å$^{-3}$. The bond energy of Ru-O bond is calculated with eq 4:[15, 16]

$$E_{\text{bond}} = E_{\text{Mono–LDH–Ru}} - E_{\text{Mono–LDH}} - E_{\text{Ru}} \quad (4)$$

where $E_{\text{Ru1/mono-NiFe}}$, $E_{\text{mono-NiFe}}$, and $E_{\text{Ru}}$ is the energy of $Ru_1$/mono-NiFe, mono-NiFe, and Ru, respectively.

During the calculating of density of states for bulk-NiFe, mono-NiFe, and $Ru_1$/mono-NiFe, the Γ-point-centered *k*-point meshes used for the Brillouin zone integrations are set as 6 × 6 × 3 in the a-, b-, and c- directions.

The oxidation of hydrazine into nitrogen and hydrogen occurs in the following six consecutive elementary steps:

(A) * + $N_2H_4$ → *$N_2H_4$,

(B) *$N_2H_4$ → *$N_2H_3$ + $H^+$ + $e^-$,

(C) *$N_2H_3$ → *$N_2H_2$ + $H^+$ + $e^-$,

(D) *$N_2H_2$ → *$N_2H$ + $H^+$ + $e^-$,

(E) *$N_2H$ → *$N_2$ + $H^+$ + $e^-$,

(F) *$N_2$ → * + $N_2$.

The asterisk (*) represents the reaction surface of these calculated LDHs. "*$N_2H_4$", "$N_2H_3$", "$N_2H_2$", "$N_2H$", and "*$N_2$" denote the models with the corresponding chemisorbed species residing in the LDHs surfaces. Among these six elementary steps, steps (A) and (F) are the adsorption of $N_2H_4$ and desorption of $N_2$, respectively. The other four elementary steps involve the generation of one proton and one electron. Then, using the computational hydrogen electrode (pH = 0, $p$ = 1 atm, $T$ = 298 K),[17] the Gibbs free energy of $H^+$ + $e^-$ was replaced implicitly with the Gibbs free energy of one-half a $H_2$ molecule. Thus the reaction Gibbs free energies can be calculated with eqs 5-10:

$$\Delta G_{\mathrm{A}} = G_{*\mathrm{N_2H_4}} \text{-} G_{*} \text{-} G_{\mathrm{N_2H_4}} \quad (5)$$

$$\Delta G_{\mathrm{B}} = G_{*N_2H_3} + 0.5G_{H_2} \text{-} G_{*N_2H_4} - eU - kT\ln 10 \cdot \mathrm{pH} \quad (6)$$

$$\Delta G_{\mathrm{C}} = G_{*\mathrm{N_2H_2}} + 0.5G_{\mathrm{H_2}} - G_{*\mathrm{N_2H_3}} - eU - kT\ln 10 \cdot \mathrm{pH} \quad (7)$$

$$\Delta G_{\mathrm{D}} = G_{*\mathrm{N_2H}} + 0.5G_{\mathrm{H_2}} - G_{*\mathrm{N_2H_2}} - eU - kT\ln 10 \cdot \mathrm{pH} \quad (8)$$

$$\Delta G_{\mathrm{E}} = G_{*\mathrm{N_2}} + 0.5G_{\mathrm{H_2}} - G_{*\mathrm{N_2H}} - eU - kT\ln 10 \cdot \mathrm{pH} \quad (9)$$

$$\Delta G_{\mathrm{F}} = G_{*} + G_{\mathrm{N_2}} - G_{*\mathrm{N_2}} \quad (10)$$

The Gibbs free energies of all reactants and products were garnered by calculating the vibrational frequencies of that molecule or intermediate.[18]

## Section 2. Supporting Figures and Tables

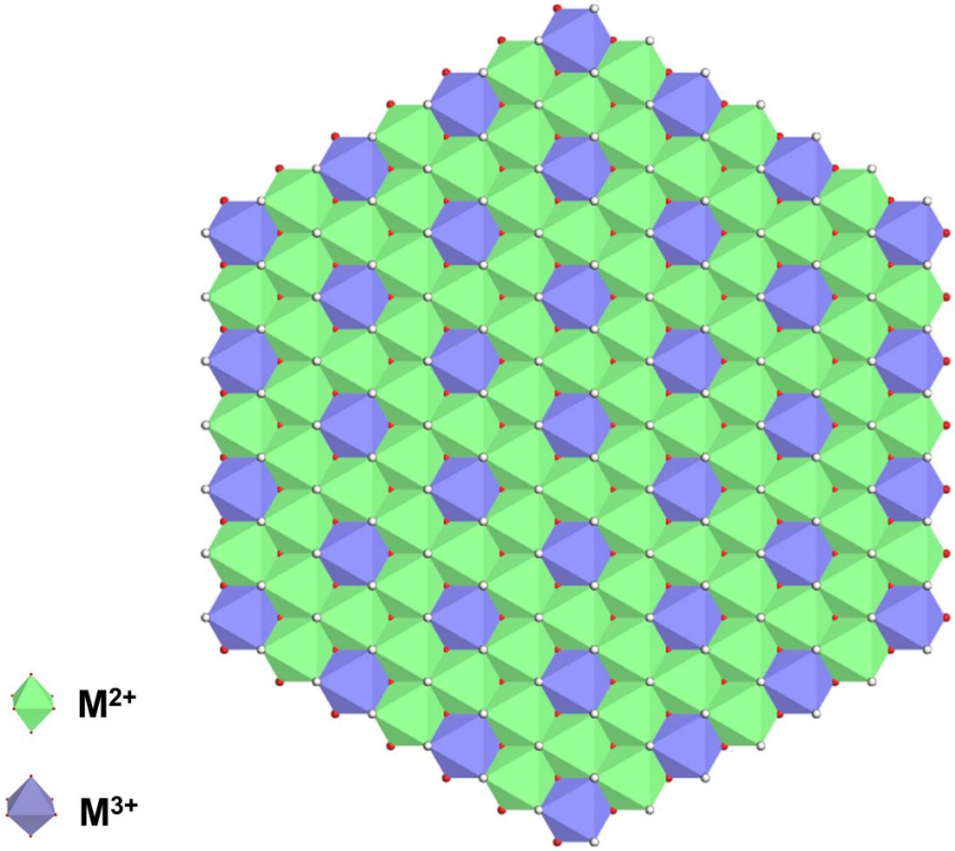


**Figure S1.** Schematic illustration of $M^{3+}$ ions dispersed by $M^{2+}$ in LDHs with the ratio of $M^{2+}/M^{3+}$ =3.

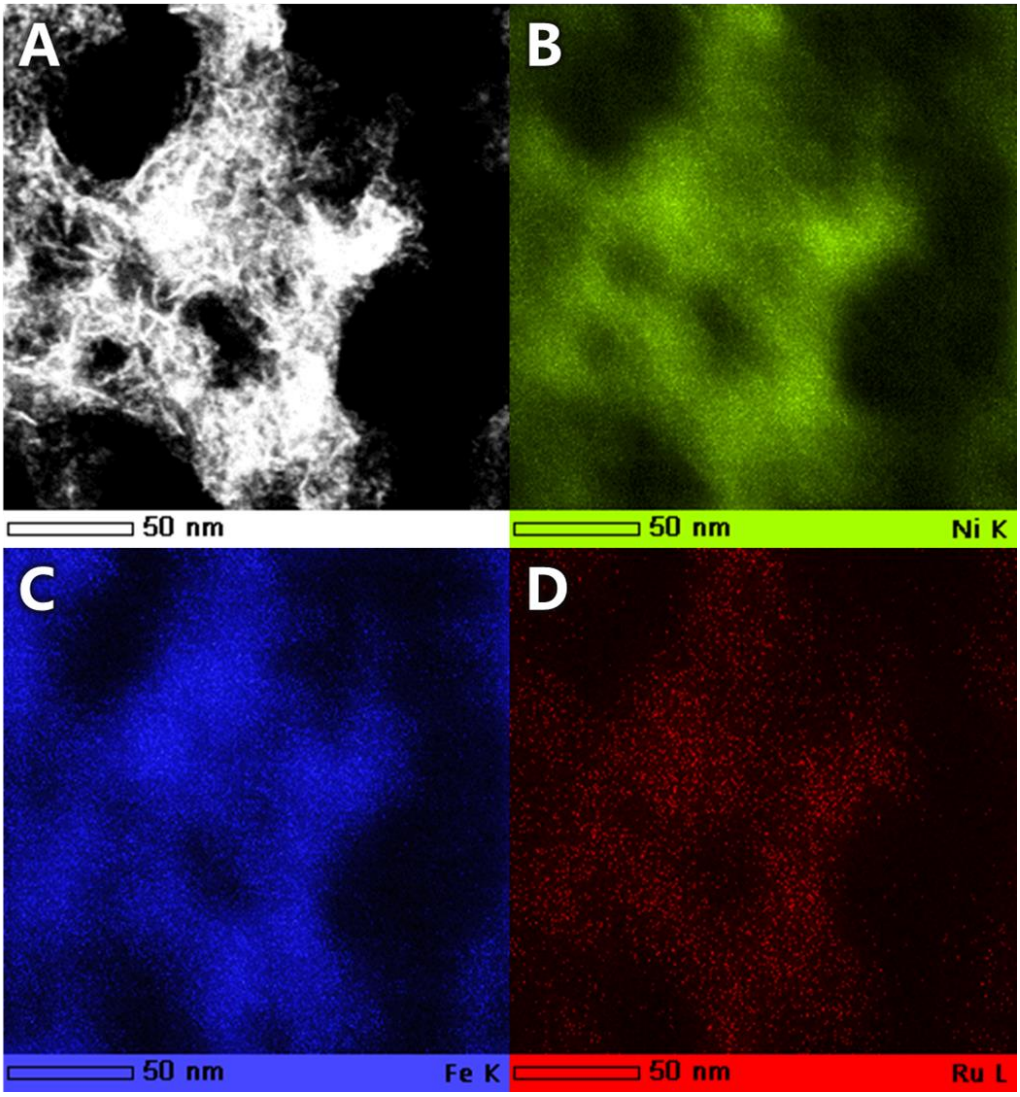


**Figure S2.** (A) STEM image of $Ru_1$/mono-NiFe-0.3 and EDS elemental mapping of $Ru_1$/mono-NiFe-0.3 for (B) Ni, (C) Fe and (D) Ru, respectively.

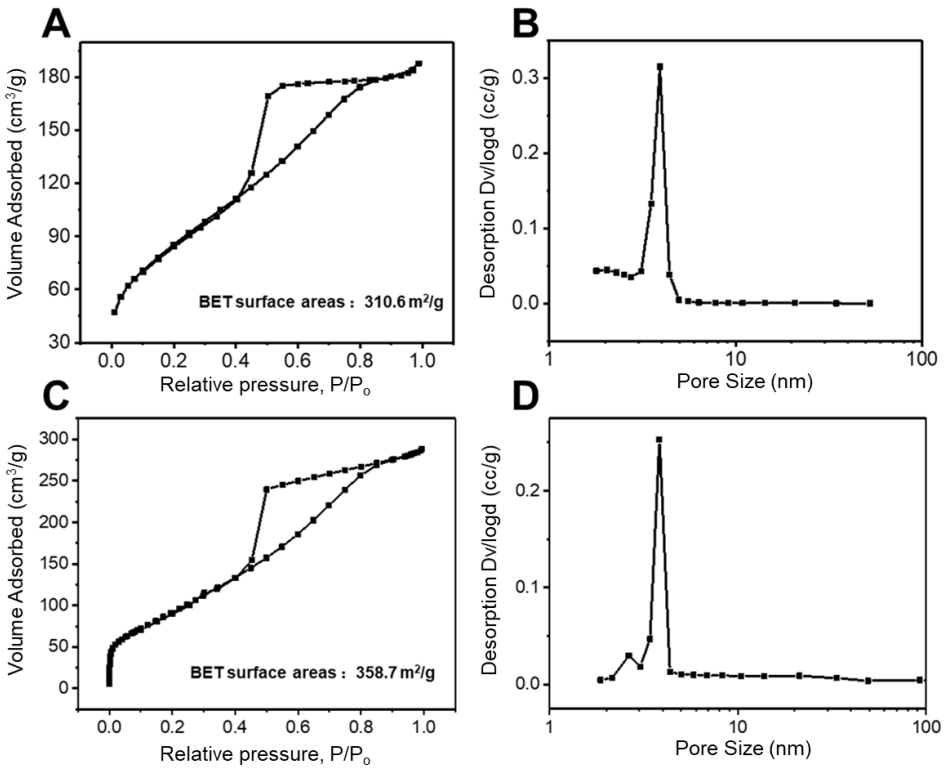


**Figure S3.** (A) $N_2$ adsorption and desorption curve and (B) distribution of pore size of mono-NiFe, (C) $N_2$ adsorption and desorption curve and (D) distribution of pore size of $Ru_1$/mono-NiFe-0.3.

The mono-NiFe possess high BET surface area of up to 310.6 $m^2/g$, which is close to the $Ru_1$/mono-NiFe-0.3 (358.7 $m^2/g$), and pore diameter of both mono-NiFe and $Ru_1$/mono-NiFe-0.3 is around ~3.7 nm.

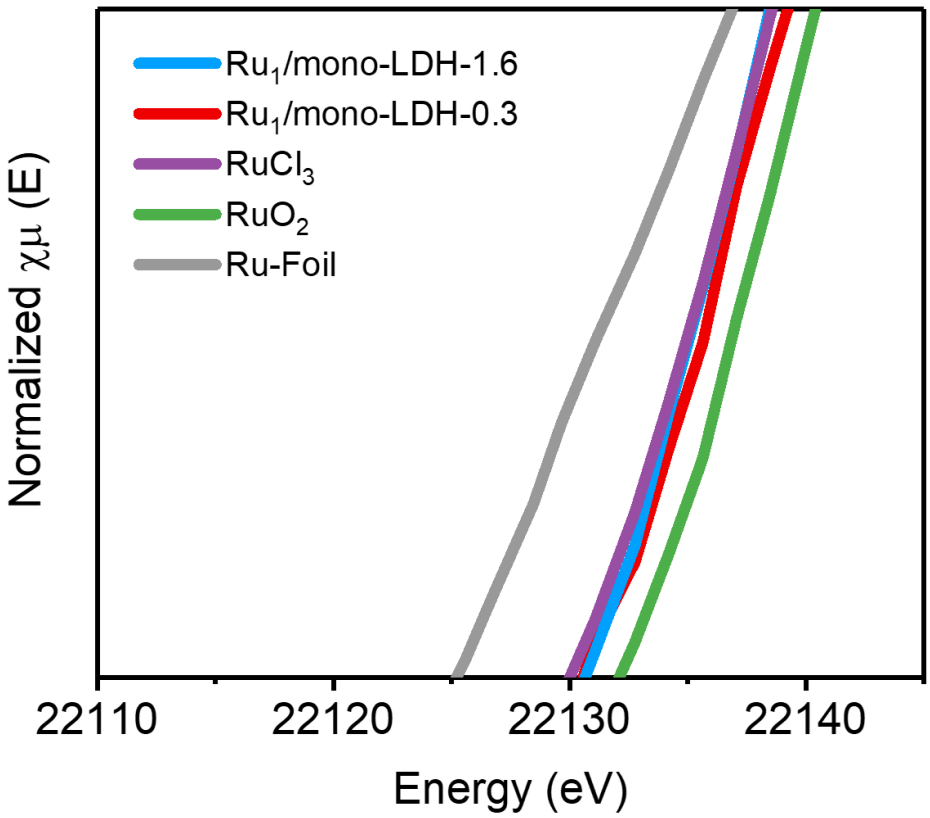


**Figure S4** Ru K-edge XANES spectra for $Ru_1$/mono-NiFe-1.6, $Ru_1$/mono-NiFe-0.3, $RuCl_3$, $RuO_2$ and Ru-foil.

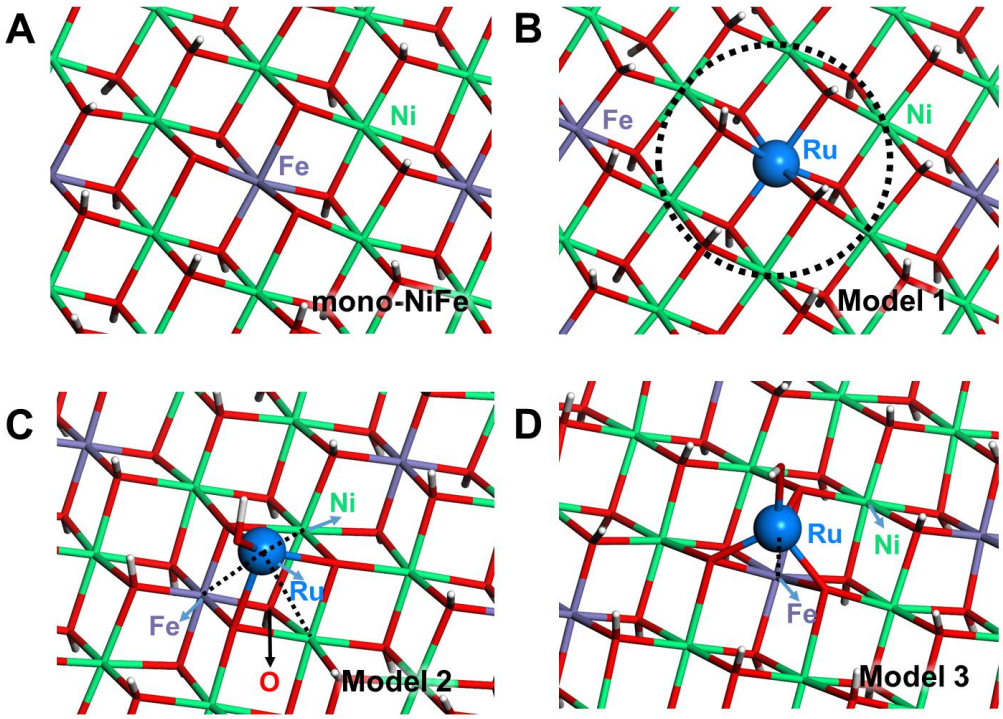


**Figure S5.** (A) schematic illustration of mono-NiFe, (B) Ru atoms are inserted/dispersed into the LDH layer (Model 1), (C) Ru ions are located upon the LDH layer and faced to the O atoms (Model 2) and (D) Ru ions are located upon the LDH layer and faced to the Ni or Fe atoms (model 3).

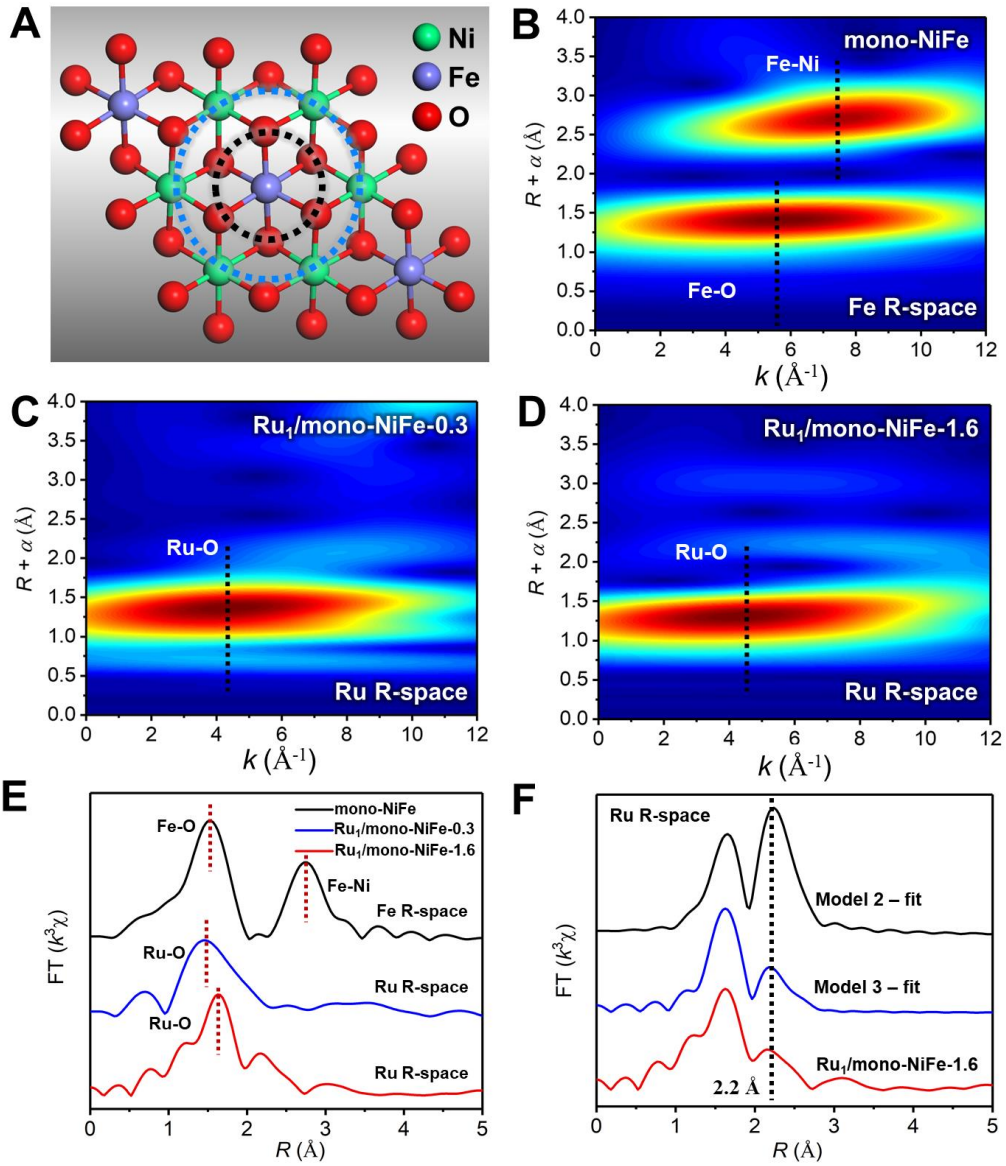


**Figure S6.** (A) schematic structure model of a mono-NiFe viewed along the c-axis; (B), (C) and (D) wavelet transforms for the $k^3$-weighted EXAFS signals of mono-NiFe (Fe R-space), $Ru_1$/mono-NiFe-0.3 (Ru R-space) and $Ru_1$/mono-NiFe-1.6 (Ru R-space) respectively; (E) magnitude of $k^3$-weighted Fourier transforms of the Ru K-edge EXAFS spectra for $Ru_1$/mono-NiFe-0.3, $Ru_1$/mono-NiFe-1.6, and Fe K-edge EXAFS spectra for mono-NiFe; (F) magnitude of $k^3$-weighted Fourier transforms of the Ru K-edge EXAFS spectra for $Ru_1$/mono-NiFe-1.6 and fitting result through model 2 and model 3.

As shown in Figure S6B, two intensity maxima at ~5.5 $Å^{-1}$ and ~7.5 $Å^{-1}$ in wavelet transform EXAFS (WT-EXAFS) can be assigned to the first Fe-O and the second Fe-Ni shell, respectively. For the $Ru_1$/mono-NiFe-0.3 and the $Ru_1$/mono-NiFe-1.6, there is only one clear intensity maxima at ~5 $Å^{-1}$ (Figure S6C, S6D), corresponding to the Ru-O coordination.

Besides, as shown in the Fe K-edge Fourier transform EXAFS (FT-EXAFS) oscillation spectra of mono-NiFe (black line) in Figure S6E, the first peak at ~1.5 Å corresponding to the Fe-O shell (Figure S6A black dashed), the second peak at ~2.7 Å corresponding to the Fe-Ni shell (Figure S6A blue dashed). The difference between $Ru_1$/mono-NiFe-*x* (*x* = 0.3, 1.6) and mono-NiFe in both WT-EXASF and FT-EXAFS gives us a specific information that the chemical environment of Ru is quite different from Fe in LDH, which means Ru atoms is not inserted into the LDH layer. In Figure S6F, the black line and the blue line are the fitting results of Model 2 (Figure S5C) and Model 3 (Figure S5D), respectively. The Model 3 gives a better fitting tendency than Model 2, which is primarily due to the different coordination atoms in the second shell. For Model 2, there are three Ni or Fe atoms coordination with Ru in the second shell, while for Model 3, there is only one atom (Ni or Fe) assigned to Ru-metal shell at 2.1 Å, the above results further indicating that the single Ru atoms are anchored upon the LDH layer and possibly tend to face the Ni or Fe atoms rather than oxygen atoms.

**Table S1.** Local structure parameters around Ru estimated by EXAFS analysis.

| Sample | Shell | $N^a$ | $R$[Å]$^b$ | $R$-factor($10^{-2}$) | $\sigma^2(10^{-2})^c$ |
|---|---|---|---|---|---|
| $Ru_1$/mono-NiFe-0.3 | Ru-O | 4.1 | 2.04±0.01 | 1.0 | 0.3 |
| $Ru_1$/mono-NiFe-1.6 | | 4.1 | 2.05±0.01 | 2.6 | 0.4 |

[a]$N$ = coordination number; [b]$R$ = average distance between absorber and backscatter atoms; [c]$\sigma^2$ = Debye-Waller factor

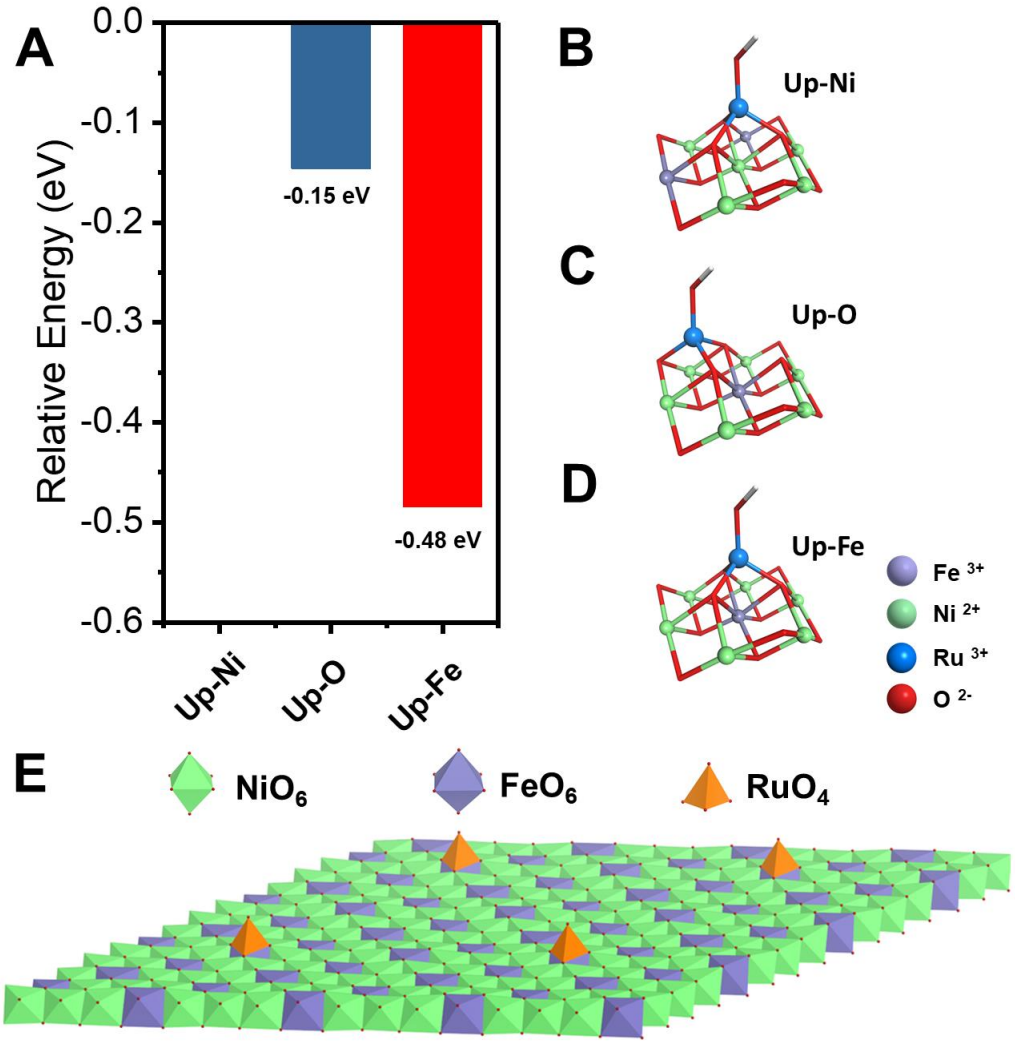


**Figure S7.** (A) relative energy of Ru atom upon the O, Ni and Fe; schematic illustration of (B) Up-Ni, (C) Up-O and (D) Up-Fe; (E) speculate structure of $Ru_1$/mono-NiFe.

Ru atom located upon the Ni atoms (denoted as Up-Ni, Figure S7B) and Ru atom located upon the Fe atoms (denoted as Up-Fe, Figure S7D) are two possible situation of Model 3 (Figure S5D), where Ru ions are localized upon the LDH layer and faced to the Ni and Fe atoms, respectively. Ru atoms located upon the O atoms (denoted as Up-O, Figure S7C) is equal to the Model 2 (Figure S5C), where Ru ions are localized upon the LDH layer and faced to the O atoms.

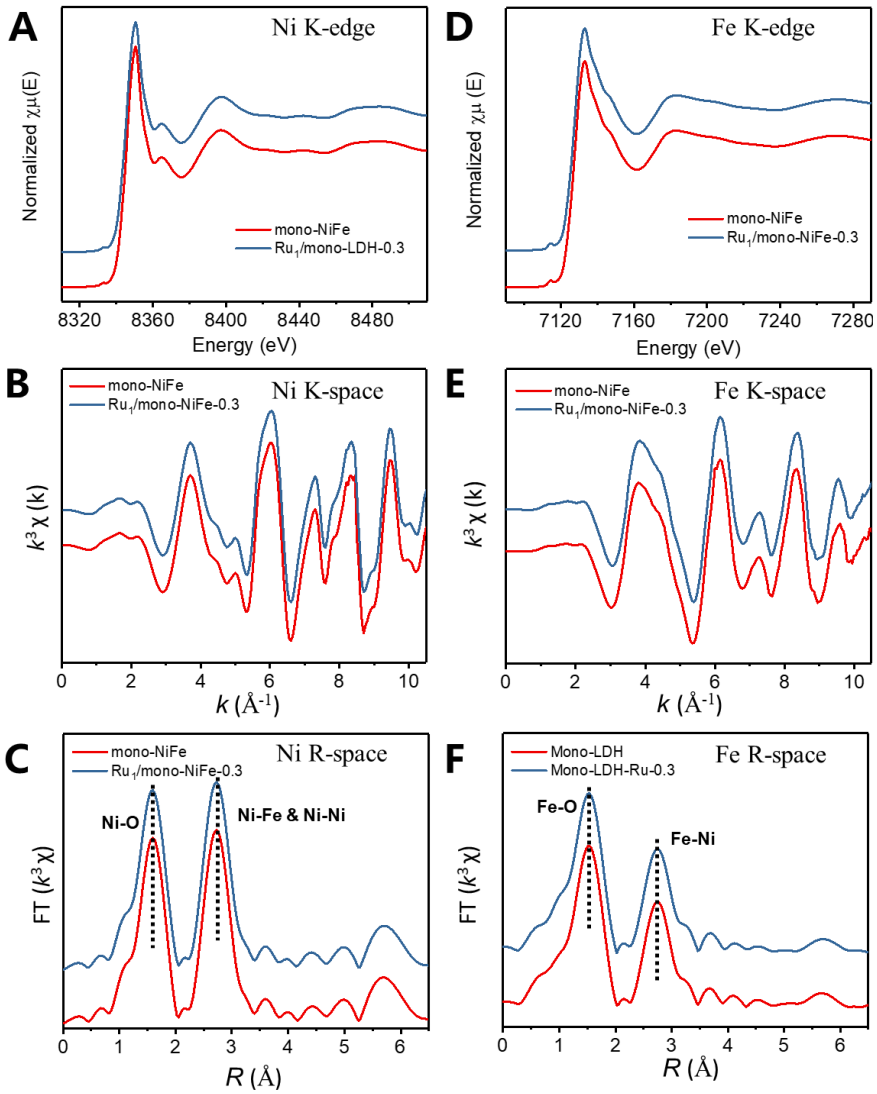


**Figure S8.** (A) Ni K-edge XANES spectra, (B) Ni K-edge EXAFS oscillation functions $k^3\chi$, and (C) magnitude of $k^3$-weighted FT of Ni K-edge EXAFS spectra; (D) Fe K-edge XANES spectra, (E) Fe K-edge EXAFS oscillation functions $k^3\chi$, and (F) magnitude of $k^3$-weighted FT of Fe K-edge EXAFS spectra for mono-NiFe, $Ru_1$/mono-NiFe-0.3, respectively.

XANES spectra and EXAFS oscillations of Ni and Fe for the mono-NiFe, $Ru_1$/mono-NiFe-0.3 shows similar spectra (Figure S8A, B, D, E), indicates the chemical environment of Ni and Fe in mono-NiFe keep the similar even after Ru loaded upon the mono-NiFe ($Ru_1$/mono-NiFe-0.3). The FT-EXAFS of the mono-NiFe and $Ru_1$/mono-NiFe-0.3 in both Ni R-space and Fe R-space (Figure S8C, F) shows two peaks corresponding to the Ni-O shell (1.6 Å) and metal-metal (2.5 Å) shells, respectively.

**Table S2.** Local structure parameters around Ru estimated by EXAFS analysis.

| Sample | | Shell | $N^a$ | $R$[Å]$^b$ | $R$-factor($10^{-2}$) | $\sigma^2$($10^{-2}$)$^c$ |
|---|---|---|---|---|---|---|
| mono-NiFe | Ni edge | Ni-O | 5.8 | 2.03±0.01 | 0.29 | 0.57 |
| $Ru_1$/mono-NiFe-0.3 | | | 5.8 | 2.03±0.01 | 0.28 | 0.58 |
| mono-NiFe | Fe edge | Fe-O | 5.7 | 1.99±0.01 | 0.42 | 0.78 |
| $Ru_1$/mono-NiFe-0.3 | | | 5.7 | 1.99±0.01 | 0.43 | 0.79 |

[a]$N$ = coordination number; [b]$R$ = average distance between absorber and backscatter atoms; [c]$\sigma^2$ = Debye-Waller factor

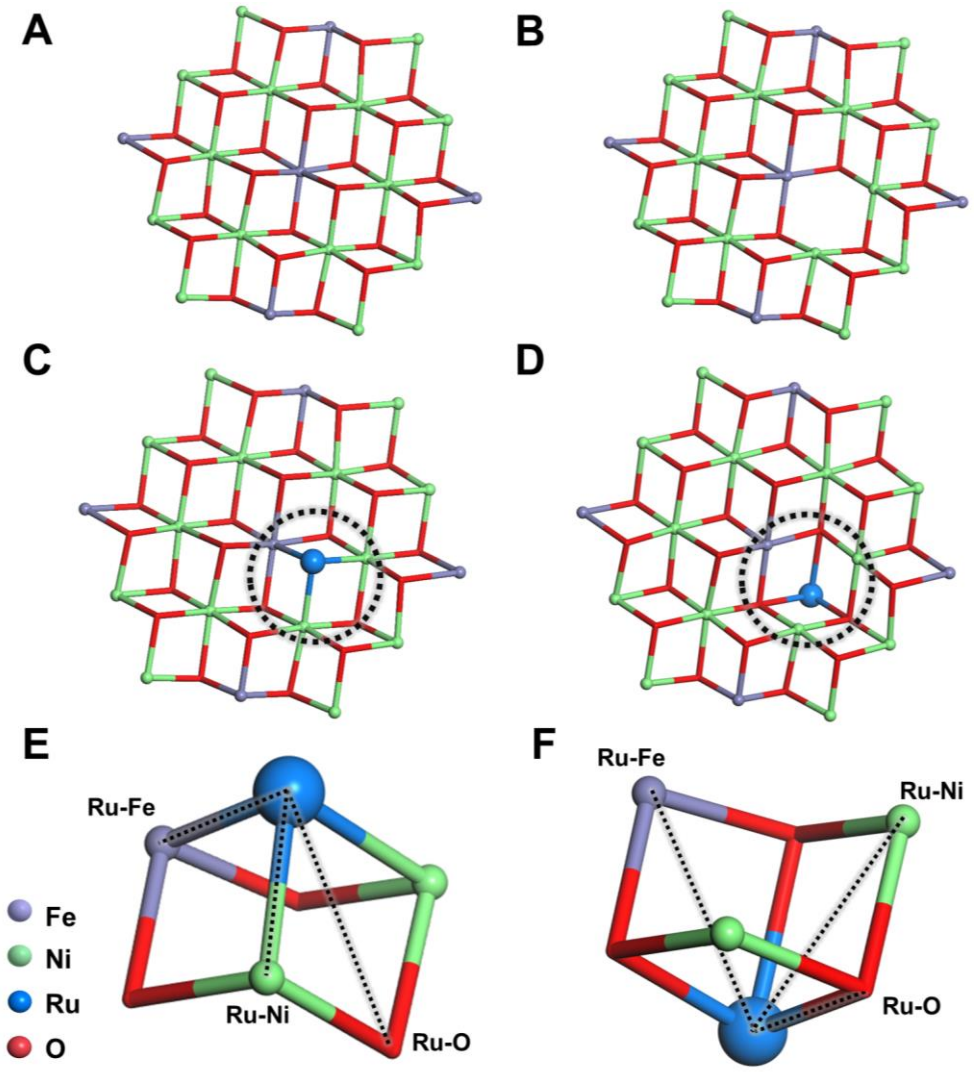


**Figure S9.** Schematic illustration of (A) the mono-NiFe; (B) the mono-NiFe with oxygen vacancy; (C) and (D) two possible position of Ru location on oxygen vacancy of the mono-NiFe; (E) and (F) the magnified image of the part marked in (C) and (D).

Very recently, some researchers reported that the surface defects can act as functional sites to stabilize single atoms.[19-21] In our work, the coordination number of both Ni-O and Fe-O in mono-NiFe is less than 6.0, indicating the existence of oxygen vacancies on the surface of monolayer LDH (Figure S9A, B). if single Ru atoms are located up to the oxygen vacancies of monolayer LDH (Figure S9C, E), the Ru-Ni/Ru-Fe bond will be formed through single Ru atom coordination with Ni/Fe atom. If single Ru atoms are located down to the oxygen vacancies of monolayer LDH (Figure S9D, F), the coordination environment is very close to the Model 2 in Figure S5C, in which the second shell of single Ru atoms coordination will include two Ru-Ni bonds and one Ru-Fe bond. The above two situations do not match with the XAFS data. As such, we can draw the conclusion the above two models are very unlikely.

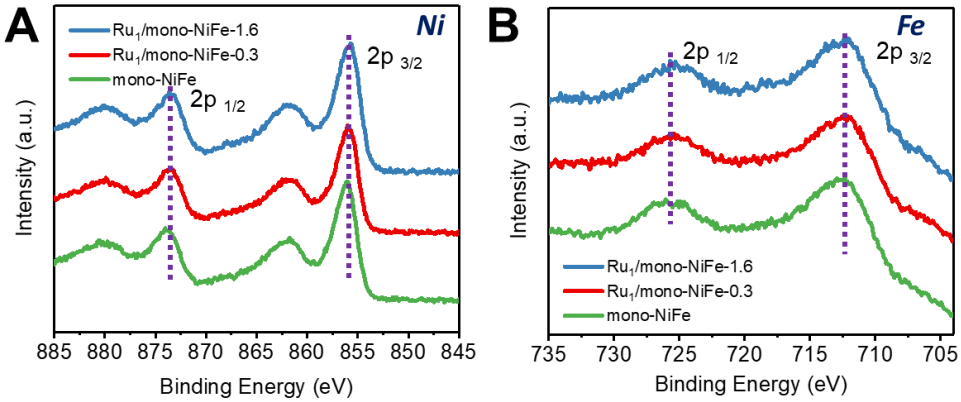


**Figure S10.** The XPS signal of (A) Ni (B) Fe for $Ru_1$/mono-NiFe-1.6, $Ru_1$/mono-NiFe-0.3, mono-NiFe, respectively.

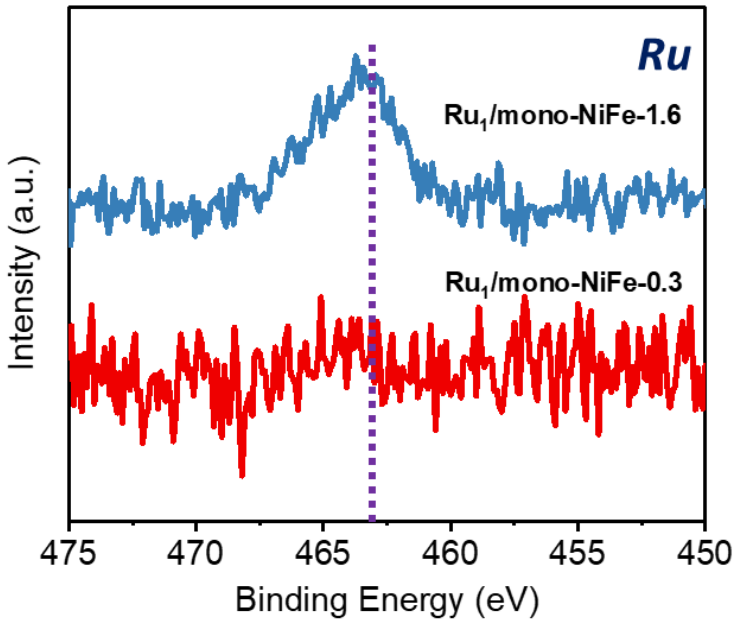


**Figure S11.** Ru XPS signal of $Ru_1$/mono-NiFe-1.6 and $Ru_1$/mono-NiFe-0.3.

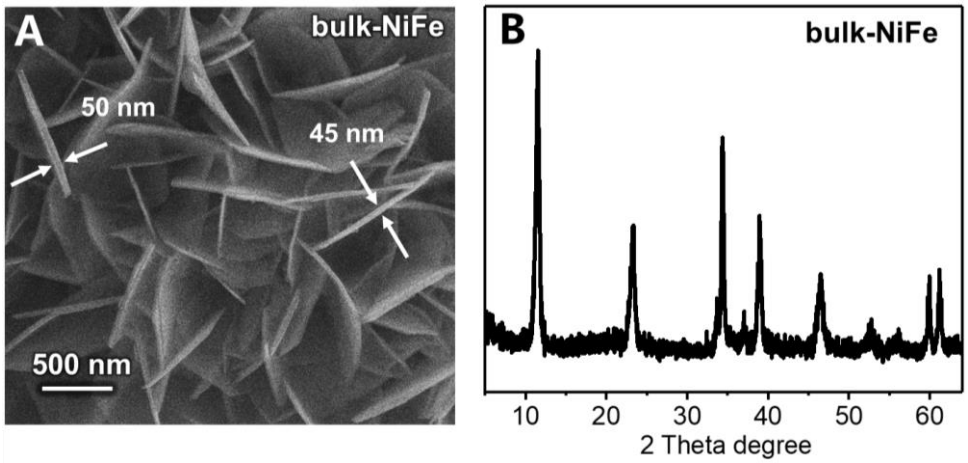


**Figure S12.** (A) SEM image and (B) XRD pattern of bulk-NiFe.

The SEM image shows the size of bulk-NiFe (Figure S11A) is 1 ~ 2 μm with the thickness of 40 ~ 50 nm. XRD (Figure S11B) also clearly shows a series of (00*l*) Bragg peaks of LDH, indicating the successful synthesis of LDH.

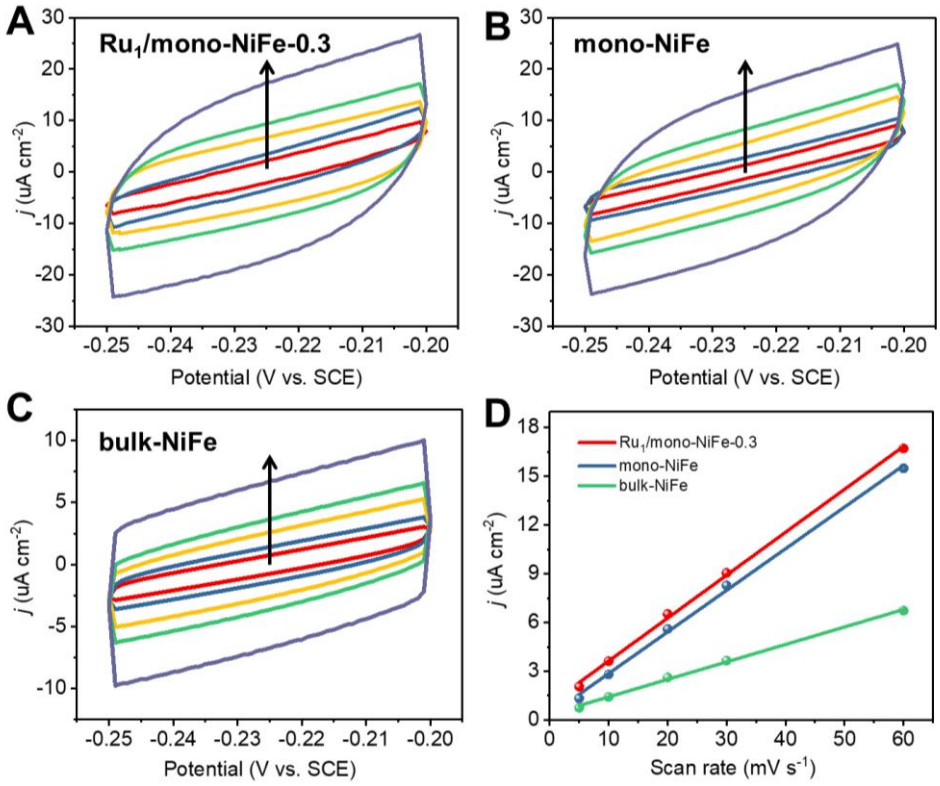


**Figure S13.** Typical CV curves of (A) $Ru_1$/mono-NiFe-0.3 (B) mono-NiFe and (C) bulk-NiFe in the mixture solution of 1 M KOH and 0.2 M $N_2H_4$ with different scan rates (5, 10, 20, 30, 60 mV $s^{-1}$); (D) charge current density differences J of $Ru_1$/mono-NiFe-0.3, mono-NiFe and bulk-NiFe based electrodes plotted against scan rate. The linear slope, equivalent to twice of the double-layer capacitance $C_{dl}$, was used to represent ECSA.

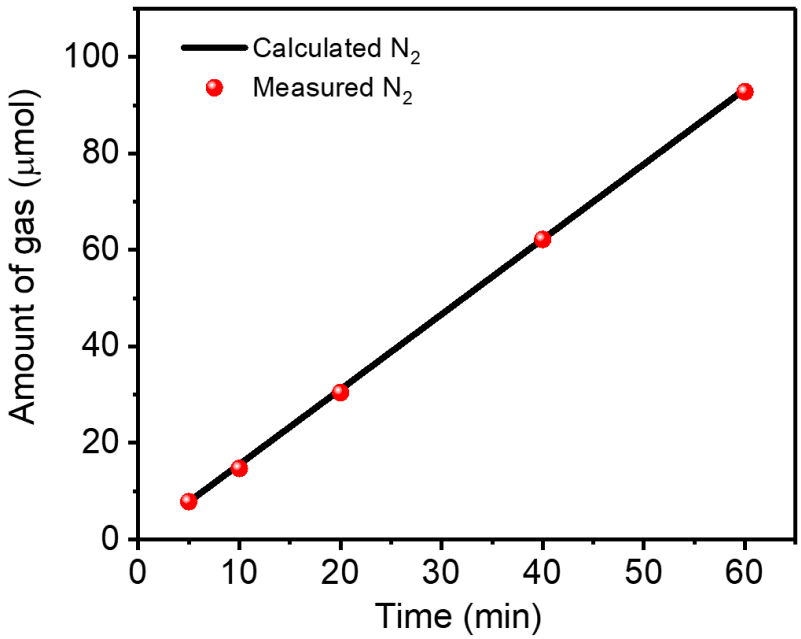


**Figure S14.** The amount of gas theoretically calculated and experimentally measured versus time for hydrazine electrooxidation of $Ru_1$/mono-NiFe-0.3.

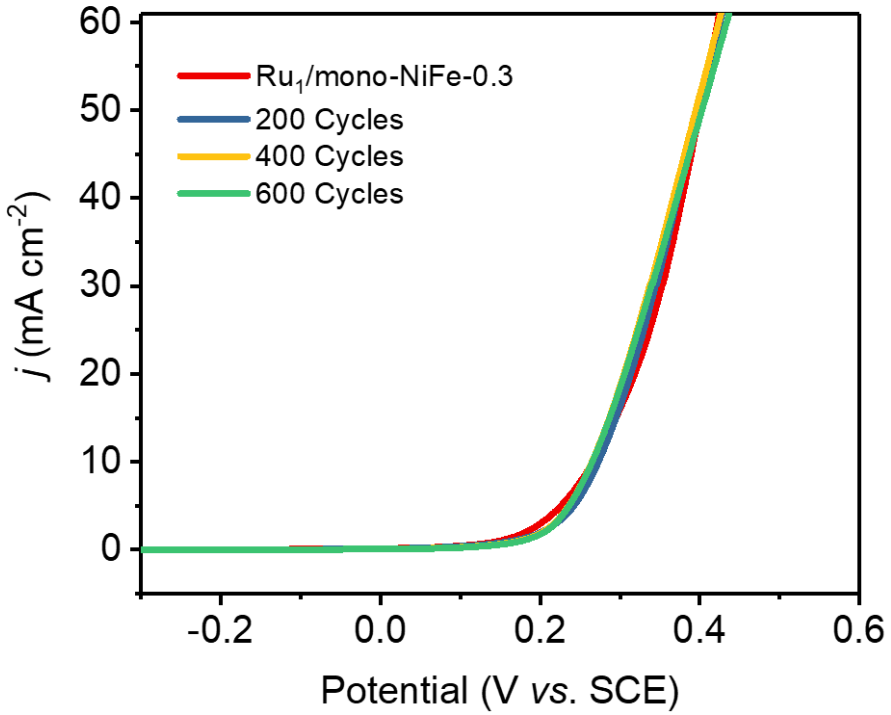


**Figure S15.** Polarization curves of $Ru_1$/mono-NiFe-0.3 before and after 600 cycles.

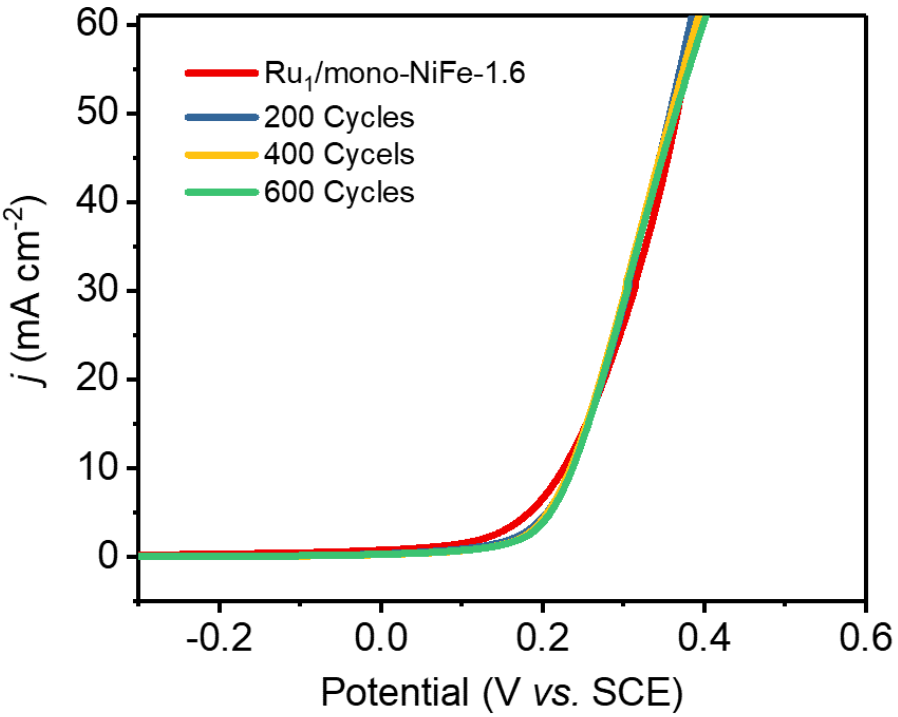


**Figure S16.** Polarization curves of $Ru_1$/mono-NiFe-1.6 before and after 600 cycles.

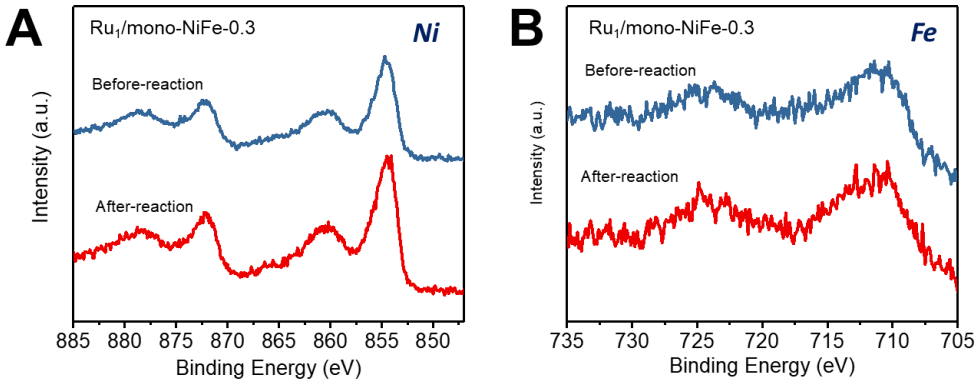


**Figure S17.** The (A) Ni (B) Fe XPS signal for $Ru_1$/mono-NiFe-0.3 before and after hydrazine electrooxidation.

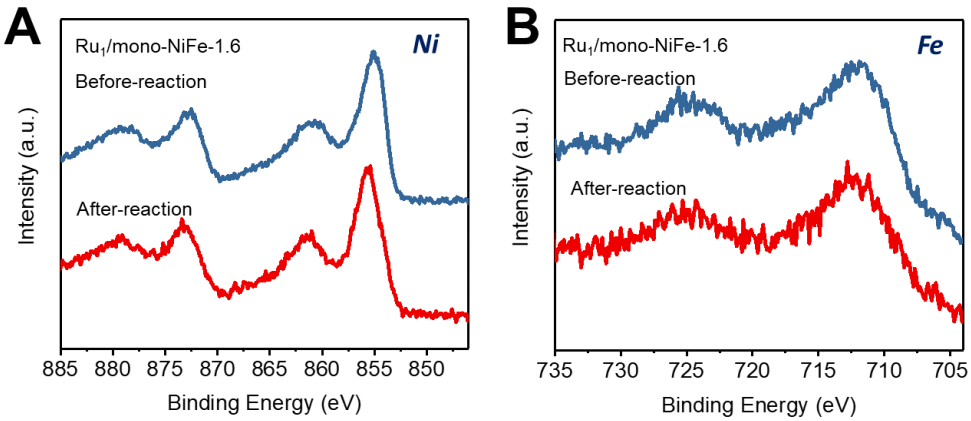


**Figure S18.** The (A) Ni (B) Fe XPS signal for $Ru_1$/mono-NiFe-1.6 before and after hydrazine electrooxidation.

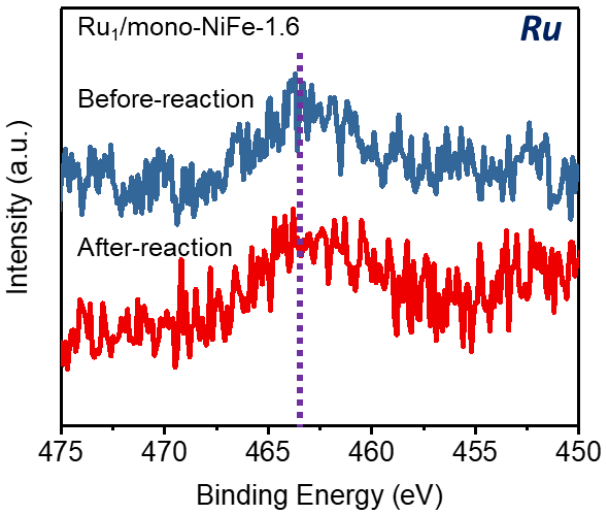


**Figure S19.** The Ru XPS signal for $Ru_1$/mono-NiFe-1.6 before and after hydrazine electrooxidation.

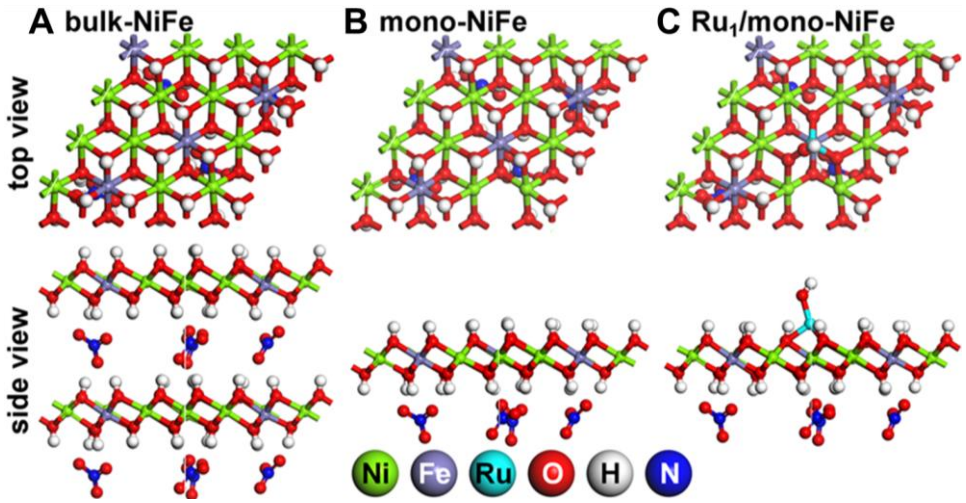


**Figure S20.** Optimized geometries of bulk-NiFe, mono-NiFe, $Ru_1$/mono-NiFe, in top view and side view, respectively. The color for each element is labeled.

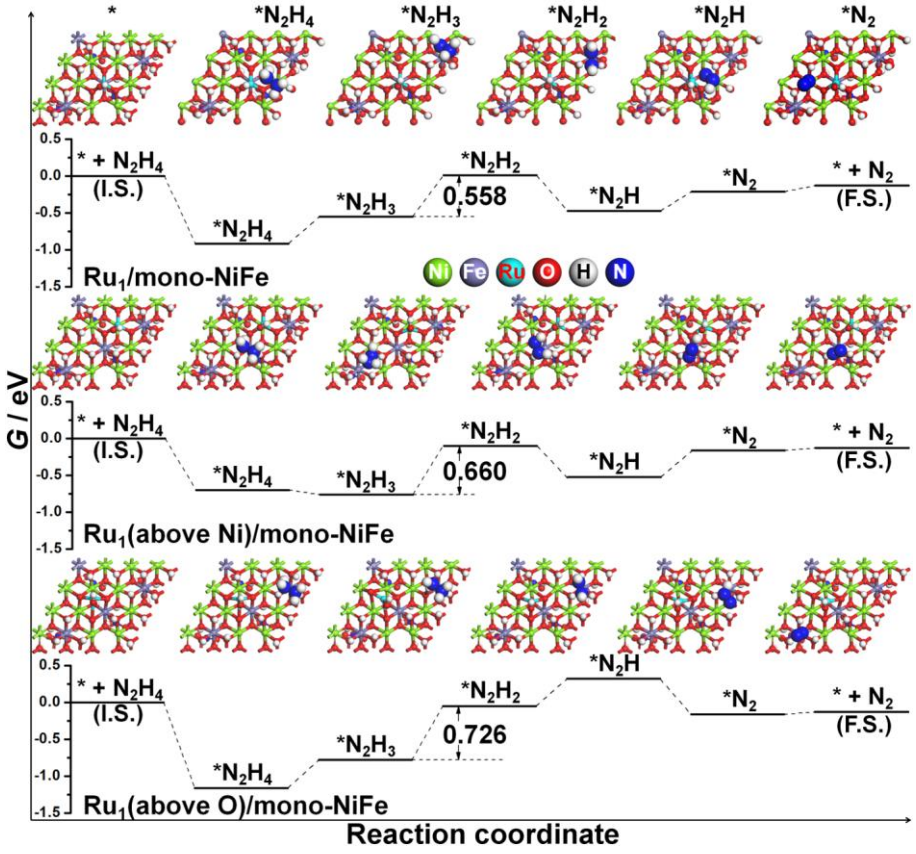


**Figure S21.** Standard free energy diagrams for the hydrazine electrooxidation on $Ru_1$/mono-NiFe, $Ru_1$(above Ni)/mono-NiFe, and $Ru_1$(above O)/mono-NiFe, respectively. Numbers here

represent the Gibbs free energy changes of the rate-determining step in hydrazine electrooxidation.

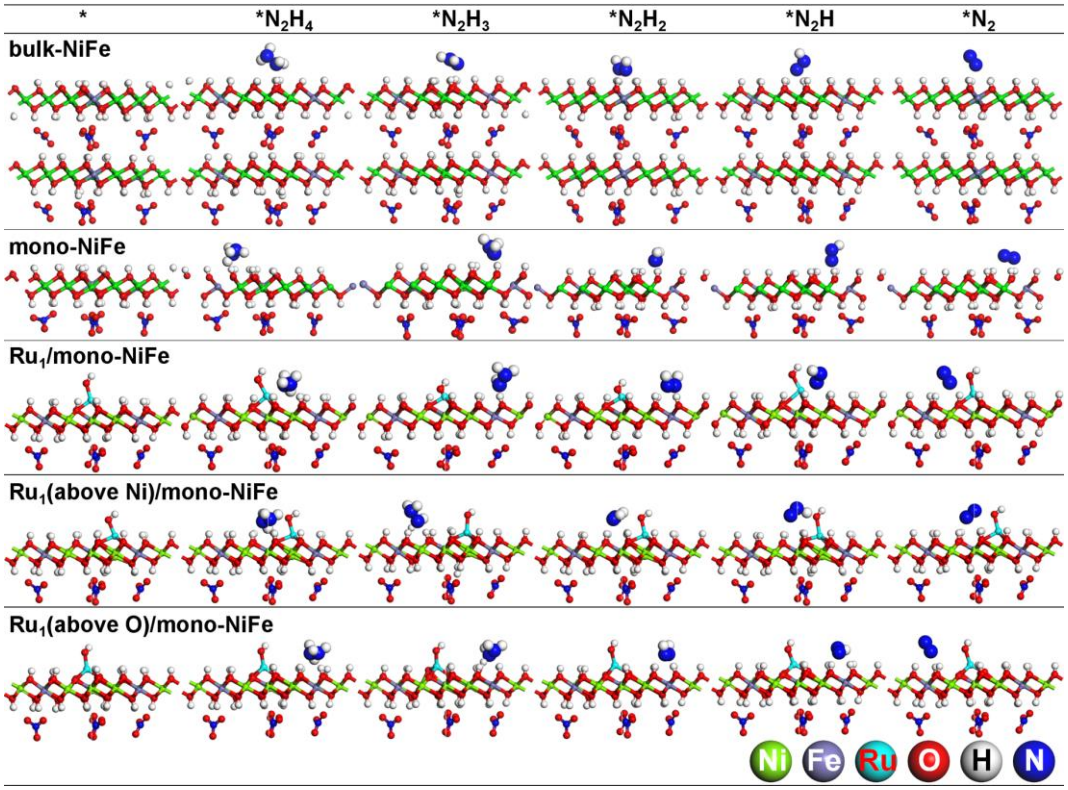


**Figure S22.** The optimized geometries for the hydrazine electrooxidation intermediates on the calculated LDHs, in the side view.

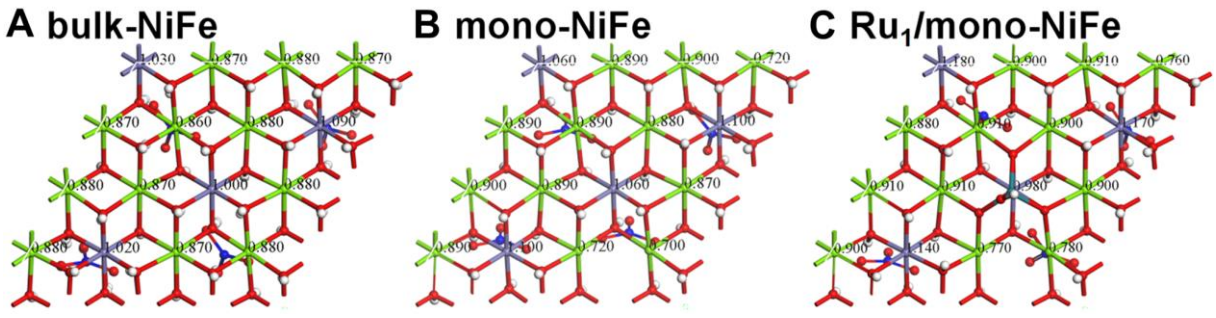


**Figure S23.** The Mulliken charge distributions for bulk-NiFe, mono-NiFe, and $Ru_1$/mono-NiFe, respectively. Numbers in the figure are the Mulliken charges with the unit of *e*. The color of each element is the same with that in Figure S22.

**Table S3.** The reaction Gibbs free energy ($\Delta G$) of each elementary step for electrocatalytic hydrazine oxidation on each calculated LDH

| elementary step | $\Delta G$ / eV | | | | | |
|---|---|---|---|---|---|---|
| | bulk-NiFe | mono-NiFe | mono-NiFe-2 | $Ru_1$/mono-NiFe | $Ru_1$/mono-NiFe-2 | $Ru_1$/mono-NiFe-3 |
| $* + N_2H_4 \rightarrow *N_2H_4$ | –0.3395 | –0.3028 | –1.2179 | –0.9153 | –0.7002 | –1.1628 |
| $*N_2H_4 \rightarrow *N_2H_3 + H^+ + e^-$ | 0.3702 | 0.5433 | 0.9212 | 0.3694 | –0.0552 | 0.3873 |
| $*N_2H_3 \rightarrow *N_2H_2 + H^+ + e^-$ | 0.3441 | 0.5367 | –1.1174 | 0.5575 | 0.6597 | 0.7258 |
| $*N_2H_2 \rightarrow *N_2H + H^+ + e^-$ | 0.7486 | 0.6960 | 0.7739 | –0.4858 | –0.4258 | 0.3689 |
| $*N_2H \rightarrow *N_2 + H^+ + e^-$ | –1.5087 | –1.7843 | 0.4709 | 0.2691 | 0.3627 | –0.4760 |
| $*N_2 \rightarrow * + N_2$ | 0.2583 | 0.1841 | 0.0423 | 0.0781 | 0.0318 | 0.0298 |

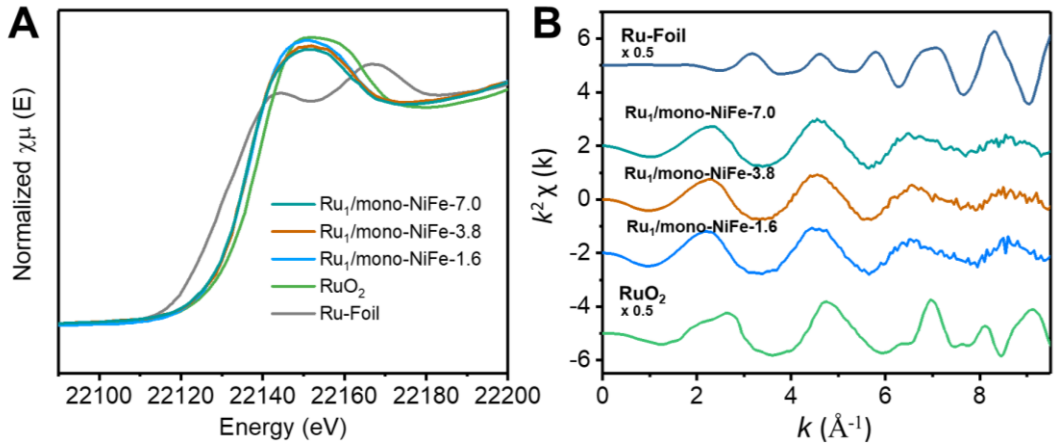


**Figure S24.** (A) Ru K-edge XANES spectra of $Ru_1$/mono-NiFe-7.0, $Ru_1$/mono-NiFe-3.8, $Ru_1$/mono-NiFe-1.6, $RuO_2$ and Ru-foil; (B) Ru K-edge EXAFS $k^2\chi$ functions of $Ru_1$/mono-NiFe-7.0, $Ru_1$/mono-NiFe-3.8, $Ru_1$/mono-NiFe-1.6, $RuO_2$ and Ru-foil.

As shown in Figure S24A, the Ru K-edge absorption positions of the $Ru_1$/mono-NiFe-7.0, $Ru_1$/mono-NiFe-3.8 and $Ru_1$/mono-NiFe-1.6, is nearly the same, smaller than $RuO_2$, indicating the +3 oxidation state of Ru. In Figure S24B, the EXAFS $k^2\chi$ functions for $Ru_1$/mono-NiFe-7.0, $Ru_1$/mono-NiFe-3.8 and $Ru_1$/mono-NiFe-1.6 quite different from those of Ru foil and $RuO_2$, with extended periods and a reduction in the oscillation amplitudes, assigned to the different coordination environment of the Ru atoms. It is believed that single Ru atoms is successfully loaded upon the mono-NiFe.

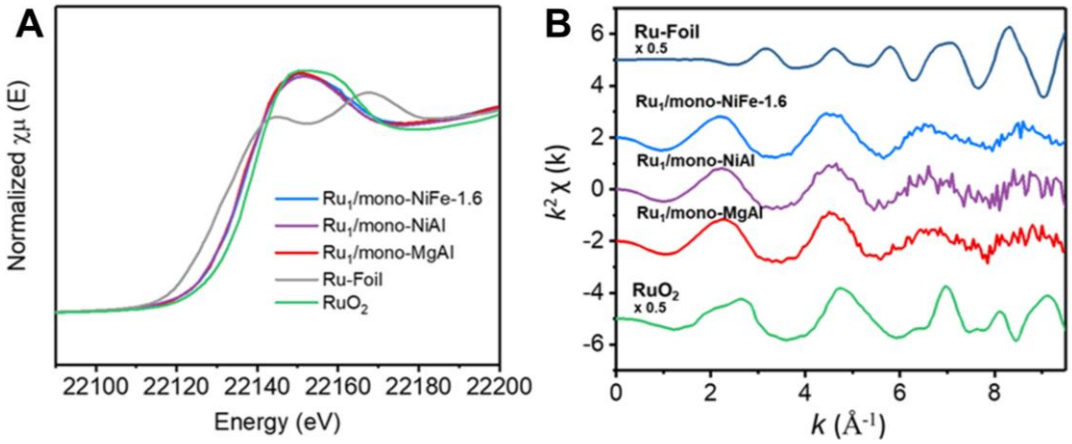


**Figure S25.** (A) Ru K-edge XANES spectra of $Ru_1$/mono-NiFe-1.6, $Ru_1$/mono-NiAl, $Ru_1$/mono-MgAl, $RuO_2$ and Ru-foil; (B) Ru K-edge EXAFS $k^2\chi$ functions for $Ru_1$/mono-NiFe-1.6, $Ru_1$/mono-NiAl, $Ru_1$/mono-MgAl, $RuO_2$ and Ru-foil.

As shown in Figure S25A, the Ru K-edge absorption positions of the $Ru_1$/mono-NiFe-1.6, $Ru_1$/mono-MgAl and $Ru_1$/mono-NiAl is nearly the same, indicating the +3 oxidation state of Ru. In Figure S25B, the EXAFS $k^2\chi$ functions for $Ru_1$/mono-NiFe-1.6, $Ru_1$/mono-MgAl and $Ru_1$/mono-NiAl are nearly the same, with the single Ru atoms located on the surface of LDH with preciously anchored upon the trivalent metal sites.

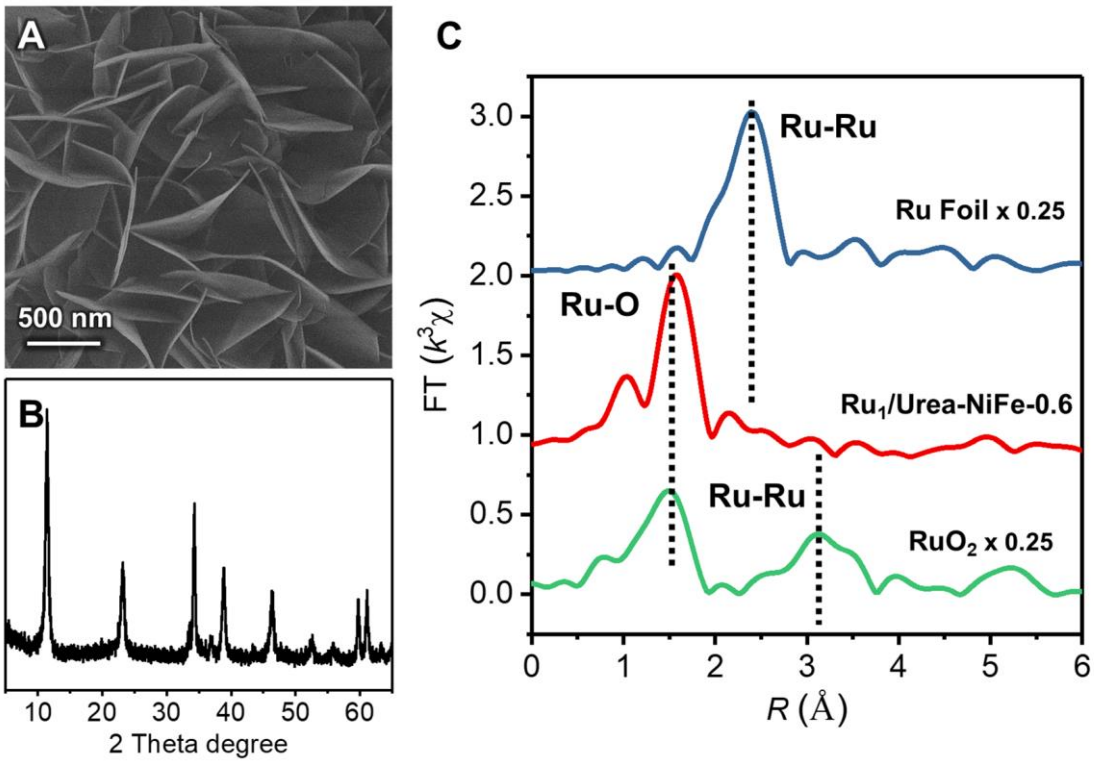


**Figure S26.** (A) SEM image and (B) XRD pattern of $Ru_1$/Urea-NiFe-0.6, (C) the magnitude of $k^2$-weighted Fourier transforms of the Ru K-edge EXAFS spectra for $Ru_1$/ultra-NiFe-0.6, $RuO_2$ and Ru-Foil.

We use the hydrothromal method to synthesize the Ru loaded LDH (Support information, experiment section). The Ru loading amount is 0.6 wt% through ICP-AES analysis (denoted as $Ru_1$/urea-NiFe-0.6). As shown in Figure S26A, the XRD data shows the typical (00*l*) basal reflection indexed to a characteristic feature of layered structure and there are no any diffractions of Ru species. The SEM images show the size of $Ru_1$/urea-NiFe-0.6 (Figure S26B) is 1 ~ 2 μm with the thickness of 40 ~ 50 nm. From XAFS result (Figure S26C), the Ru atoms on the $Ru_1$/urea-NiFe-0.6 is located on the surface of LDH and single atomically dispersed. Based on the above result, there is no obvious connection between the synthesis method and the Ru location on LDH in this case.

# References


1. B. Ravel and M. Newville, *J. Synchrotron Radiat*, 2005, **12**, 537.
2. M. Munoz, P. Argoul and F. Farges, *Am. Mineral.*, 2003, **88**, 694.
3. J. Yu, B. R. Martin, A. Clearfield, Z. Luo and L. Sun, *Nanoscale*, 2015, **7**, 9448.
4. M. C. Payne, M. P. Teter, D. C. Allan, T. A. Arias and J. D. Joannopoulos, *Rev. Mod. Phys.*, 1992, **64**, 1045.
5. M. D. Segall, P. J. D. Lindan, M. J. Probert, C. J. Pickard, P. J. Hasnip, S. J. Clark and M. C. Payne, *J. Phys-Condens. Mat.*, 2002, **14**, 2717.
6. J. P. Perdew, K. Burke and M. Ernzerhof, *Phys. Rev. Lett.*, 1996, **77**, 3865.
7. P. Liao, J. A. Keith and E. A. Carter, *J. Am. Chem. Soc.*, 2012, **134**, 13296.
8. N. Alidoust, M. C. Toroker and E. A. Carter, *J. Phys. Chem. B*, 2014, **118**, 7963.
9. N. J. Mosey, P. Liao and E. A. Carter, *J. Chem. Phys.*, 2008, **129**, 014103.
10. K. G. Reeves and Y. Kanai, *J. Chem. Phys.*, 2014, **141**, 024305.
11. M. Bajdich, M. Garcia-Mota, A. Vojvodic, J. K. Norskov and A. T. Bell, *J. Am. Chem. Soc.*, 2013, **135**, 13521.
12. M. Garc á-Mota, M. Bajdich, V. Viswanathan, A. Vojvodic, A. T. Bell and J. K. Nørskov, *J. Phys. Chem. C*, 2012, **116**, 21077.
13. L. M. Anglada and J. M. Bofill, *J. Comput. Chem.*, 1998.
14. S.-M. Xu, H. Yan and M. Wei, *J. Phys. Chem. C*, 2017, **121**, 2683.
15. J. A. Phillips, S. J. Danforth, N. J. Hora, J. R. Lanska and A. W. Waller, *J. Phys. Chem. A*, 2017, **121**, 9252.
16. M. Blasko, P. Mach, A. Antusek and M. Urban, *J. Phys. Chem. A*, 2018, **122**, 1496.
17. J. K. Nørskov, J. Rossmeisl, A. Logadottir, L. Lindqvist, J. R. Kitchin, T. Bilgaard and H. Jonsson, *J. Phys. Chem. B*, 2004, **108**, 17886.
18. E. B. Wilson, J. C. Decius and P. C. Cross, *Dover: New York*, 1980.
19. L. Zhang, J. Fischer, Y. Jia, X. Yan, W. Xu, X. Wang, J. Chen, D. Yang, H. Liu, L. Zhuang, M. Hankel, D. J. Searles, K. Huang, S. Feng, C. L. Brown and X. Yao, *J. Am. Chem. Soc.*, 2018, **140**, 10757.
20. L. Zhang, Y. Jia, G. Gao, X. Yan, N. Chen, J. Chen, M. T. Soo, B. Wood, D. Yang, A. Du and X. Yao, *Chem*, 2018, **4**, 285.
21. J. Wan, W. Chen, C. Jia, L. Zheng, J. Dong, X. Zheng, Y. Wang, W. Yan, C. Chen, Q. Peng, D. Wang and Y. Li, *Adv. Mater.*, 2018, **30**, 1705369.